sciendo

Transactions on Aerospace Research eISSN 2545-2835, VOL. 271, NO. 2/2023, 1-16
DOI: 10.2478/tar-2023-0007

CFD STUDY OF BASE DRAG OF THE GROT ROCKET

Nezar Sahbon[*1], **Maciej Michałów**[2], **Siddharth Murpani**[1], **Paulina Żurawka**[1], **Kacper Kaczmarek**[1]

[1] Student's Space Association, Faculty of Power and Aeronautical Engineering, Warsaw University of Technology, Nowowiejska 24, 00-665 Warsaw, Poland

[2] ISAE-SUPAERO, University of Toulouse, 10 Av. Edouard Belin, 31400 Toulouse, France

Abstract

Propulsion system operation is known to affect the aerodynamic characteristics of rockets. Specifically, the net axial force acting on a rocket in flight cannot be precisely obtained by combining the static thrust with drag values computed for a rocket with an inactive motor. One of the main reasons for this is the influence of motor operation on pressure at the base of the rocket. The aim of this paper is to investigate the effect of motor operation on the aerodynamic parameters of the Grot sounding rocket developed by the Students' Space Association, Warsaw University of Technology. The study consists of two series of axisymmetrical computational fluid dynamic simulations of flow around the rocket – one with the motor being non-operational and the other with active thrust. In the post-processing phase, the axial force acting on various components of the rocket is computed, with an emphasis on the base and nozzle exit sections. Quantitative and qualitative differences between the cases with and without active thrust are highlighted and discussed. The obtained results are compared to a semi-empirical model found in the literature. Finally, a semi-empirical base drag model is proposed for use in Grot flight simulation.

Keywords: base drag; computational fluid dynamics; rocket aerodynamics; sounding rockets; solid rocket propulsion

Type of the work: research article

Nomenclature

A_e	– nozzle exit area
C_D	– drag coefficient
C_{DB}	– base drag coefficient
C_{DA}	– aft part drag coefficient
D	– total drag force
D_R	– drag acting on the rocket excluding the nozzle exit
D_N	– pressure drag acting on the nozzle exit
F_T	– total axial force vector
$\dot{m}$	– mass flow rate of exhaust gases at the nozzle exit
$\cdot^{on}$	– parameter computed for the operational propulsion system
$\cdot^{off}$	– parameter computed for the non-operational propulsion system
p	– pressure at the nozzle exit

This work is licensed under a Creative Commons Attribution-NonCommercial-NoDerivatives 4.0 International License.

* Corresponding Author: nezar_ammar_miloud.sahbon.stud@pw.edu.pl

ARTICLE HISTORY **Received** 2022-04-24 **Revised** 2022-11-22 **Accepted** 2023-03-02

p_a – atmospheric pressure
$\frac{d\vec{p}}{dt}$ – rate of change of momentum
S_{ref} – reference surface area
$\vec{T}$ – thrust force vector
T_a – ambient temperature
$\vec{v}_e$ – axial velocity vector at the nozzle exit
$\vec{v}_\infty$ – far field velocity vector
$\Delta\vec{D}$ – difference in drag force between operational and non-operational propulsion systems
ρ – density at the nozzle exit
∂S – nozzle exit Surface

INTRODUCTION

Aerodynamic analysis is crucial to aerospace vehicle design and development. Accurate prediction of the performance from an aerodynamics point of view provides an edge during the design process and simulations prior to flight. A classical approach for accurate prediction of the aerodynamic characteristics is aerodynamic wind tunnel experimentation. Another valuable source of data involves the use of computational fluid dynamics (CFD), since it is not reliant on expensive infrastructure and gives insight into phenomena that may be difficult to capture with wind tunnel experiments. In the case of rocket aerodynamics, both approaches have been widely applied.

The Grot sounding rocket's main design objective was maximising the apogee; thus, accurate performance estimation was an important aspect of design and mission analysis. In order to obtain more realistic results, it was of interest to investigate the impact of the propulsion system operation on the overall aerodynamics.

In general, it is not possible to accurately obtain the net axial force acting on an in-flight rocket by simply adding the static thrust to the drag value calculated for a rocket with a non-operational propulsion system. This phenomenon is often related to a change in pressure acting on the rear of the rocket; this pressure creates a drag component commonly known as base drag [1].

In the analysis of base drag, several approaches and methodologies have been utilised in the literature to obtain valid results. Moore et al. [2] utilised wind tunnel experiments to investigate the impact of angle of attack, fin deflection, fin location and fin thickness on base drag, in an attempt to extend the Brazzel and Henerson [3] technique. Huffman [4], in his work, outlined a mathematical model for axial force coefficient calculation based on effects from overall pressure influence, base drag and friction drag. The mathematical model outlined the base drag for power-on and power-off conditions for differing Mach regimes. Al-Obaidi [5] performed drag prediction for bodies flying at supersonic speeds. The drag constituents taken into account were skin friction drag, base drag and wing-body interference drag. A coherent relationship between the base drag coefficient and the base pressure coefficient was established. The paper concluded that classical panel methods are not able to capture the effects of base drag; however, modified panel methods may be used. Kumar [6] outlined an improved method for prediction of motor-on base drag and overall drag of a rocket. Furthermore, the paper claimed expansion of a pre-existing Brazzel's method to a high thrust coefficient and Mach number range. The classical method (Brazzel's method) and the improved semi-empirical model were compared. It was concluded that they yield numerically similar results, supporting the use of CFD for accurate modelling of the physics behind the flow.

The purpose of this paper is to study the effect of engine operation on the aerodynamic performance of the Grot sounding rocket. This purpose is achieved by the use of CFD computations. Furthermore, a comparison of CFD results and an analytical model found in the literature is performed. It is expected that the models would not completely coincide, since the Grot sounding rocket has an unusual aft geometry and two stages with significantly different calibres.

2. BACKGROUND

2.1. Grot sounding rocket

The rocket used for the study is a sounding rocket developed by the Students' Space Association, known as Grot. Grot is a 2-m-long dart-type rocket (Fig. 1), which comprises two stages. The first stage accelerates the dart (second stage) to an altitude of 2 km, where aerodynamic separation takes place and the motor (first stage) plunges back to the ground, while the dart continues flying to an altitude of 18.5 km. Key parameters describing the Grot sounding rocket can be found in Table 1.

Table 1. Grot main dimensional parameters.

Parameter	**Value [m]**
Total rocket length	2.000
First stage length	0.983
Second stage length	1.017
First stage diameter	0.135
Second stage diameter	0.045
Reference diameter	0.135
Pre-flight distance of centre of mass from the rocket's base	0.979
Nozzle exit diameter	0.084

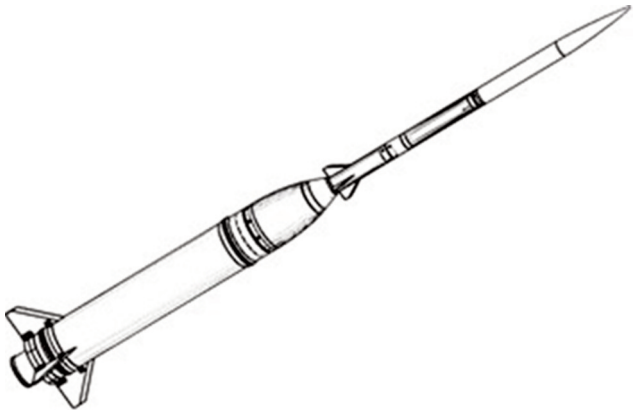


Figure 1. Visualisation of the Grot sounding rocket.

2.2. Conical rocket nozzles

Various types of nozzles have found use in rocketry; most configurations consist of converging and diverging sections, with the throat located at the minimal cross-sectional area. The variations between the types usually concern the diverging section, as it is determined to be the most crucial for achieving high performance.

The conical nozzle (Fig. 2) is one of the simplest and oldest geometries. One can define a theoretical correction factor λ [7] for the ideal conical rocket nozzle:

$$\lambda = \frac{1}{2}\left(1+\cos\alpha\right) \tag{1}$$

where α is the divergence cone angle. The correction factor determines the ratio between the momentum of the gases in a nozzle with a nozzle angle 2α and the momentum of an ideal nozzle with all gases flowing in the axial direction. It should be noted that it applies only to the momentum thrust, not the pressure thrust.

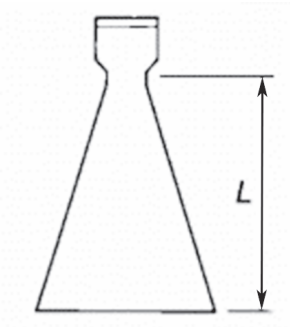


Figure 2. Conical rocket nozzle [7].

Large divergence angles enable light and short designs at the expense of performance, while small angles lead to the majority of the momentum being axial, which in turn improves the specific impulse, but the increased length influences the complexity of the design and the weight of the propulsion system and vehicle. The optimal setting is usually found to have a half-angle between 12° and 18°, depending on the application and mission profile. The Grot rocket uses a conical nozzle with a half-angle of 15°.

2.3. Thrust of a rocket motor

Thrust is a reaction force generated when an exhaust plume is ejected from a motor; this in turn applies a force pushing the motor in the opposite direction, as described by Newton's third law. The inertial term of the thrust equation can be derived from Newton's second law, as shown in Eq. (2):

$$\vec{F} = \frac{d\vec{p}}{dt} \rightarrow \vec{F} = \frac{d\left(m\vec{v}\right)}{dt} \rightarrow F = \dot{m}\vec{v}. \tag{2}$$

An additional source of thrust is the pressure force acting on the nozzle exit. The full thrust force equation for a rocket motor can be seen in Eq. (3).

$$\vec{T} = \dot{m}\cdot\vec{v}_e + \left(p - p_a\right)A_e \rightarrow T = p\cdot\vec{v}_e\cdot\left|\vec{v}_e\right|\cdot A_e + \left(p - p_a\right)A_e. \tag{3}$$

In the more accurate integral form, Eq. (3) can be presented as Eq. (4):

$$\vec{T} = -\int_{\partial\tau} \rho \cdot \vec{v}_e \cdot |\vec{v}_e| \, dS - \int_{\partial\tau} (p - p_a) \, dS. \tag{4}$$

For an ideally expanded nozzle, the second term tends to zero; nozzle expansions are illustrated in Fig. 3.

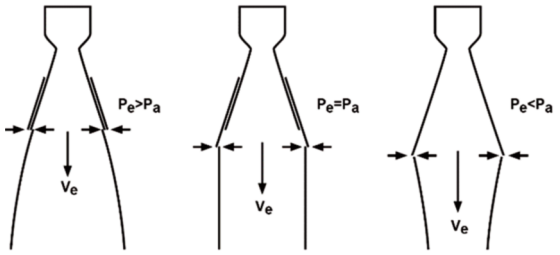


Figure 3. From left to right: (A) under-expanded nozzle, (B) ideally expanded nozzle and (C) over-expanded nozzle; based on http://www.braeunig.us/space/sup1.htm.

2.4. Definition of axial forces

The Grot sounding rocket with the directions of the relevant axial forces is shown in Fig. 4. In the following discussions, it shall always be assumed that any component of drag is defined as positive when acting in the direction of the flow velocity $\vec{v}_\infty$ (i.e. slowing the rocket down).

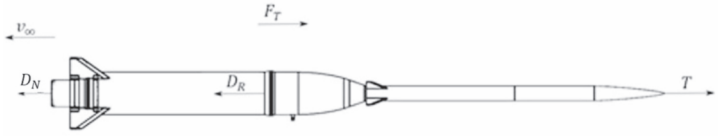


Figure 4. Axial forces acting on the Grot rocket.

The axial forces present during the flight of the rocket vary depending on the Mach number and operation status of the propulsion system. Therefore, two cases were distinguished, the first being the non-operational propulsion system and the second being the operational propulsion system.

2.4.1. Non-operational propulsion system

When the propulsion system is inactive, the only external force acting on the rocket is the drag. By definition, drag is assumed to be positive when acting in the direction of the airflow. The total axial forces in the case of a non-operational motor are presented in Eq. (5):

$$\vec{F}_T^{off} = -\vec{D}^{off} = -\vec{D}_R^{off} - \vec{D}_N^{off}, \tag{5}$$

where:

$\vec{F}_T^{off}$ – total axial force acting on the rocket for the non-operational propulsion system;

$\vec{D}^{off}$ – total drag for the non-operational propulsion system;

$\vec{D}_R^{off}$ – drag acting on the rocket excluding the nozzle exit for the non-operational propulsion system;

$\vec{D}_N^{off}$ – pressure drag acting on the nozzle exit, computed using the area integral (as shown in Eq. (6)).

$$\vec{D}_N^{off} = -\int_{\partial\tau} (p - p_a) dS. \tag{6}$$

The common approach in analysis of aerodynamic characteristics is to use coefficients instead of the forces. The drag coefficient is defined in Eq. (7):

$$\vec{D} = \frac{1}{2}\rho v^2 S_{ref} C_D \rightarrow C_D = \frac{2|\vec{D}|}{\rho v^2 S_{ref}}. \tag{7}$$

The coefficients of other discussed forces were computed analogously.

2.4.2. Operational propulsion system

While the motor is in the operational state, the thrust force generated by the exhaust plume propels the rocket forward during flight and the drag force acts in the opposite direction. The total axial force, Fon, is expressed by Eq. (8):

$$\vec{T}_T^{on} = \vec{T} - \vec{D}_T^{on} = \vec{T} - \vec{D}_R^{on}, \tag{8}$$

where:

$\vec{D}^{on}$ – total drag for the operational propulsion system

$\vec{D}_R^{on}$ – drag acting on the rocket excluding the base for the operational propulsion system (note that the pressure force acting on the base is already incorporated in the definition of thrust in Eq. (4); therefore, $\vec{D}^{on} = \vec{D}_R^{on}$).

The drag in the engine-on case can be expressed as follows:

$$\vec{D}^{on} = \vec{D}_R^{on} = \vec{D}^{off} - \Delta\vec{D}. \tag{9}$$

In Eq. (9), $\Delta\vec{D}$ is the difference between the drags acting on the rocket with active and inactive propulsion systems. It is useful to express $\Delta\vec{D}$ by rearranging Eq. (6):

$$\Delta\vec{D} = \vec{D}_N^{off} + \vec{D}_R^{off} - \vec{D}_R^{on}.$$

The difference $\vec{D}_R^{off} - \vec{D}_R^{on}$ is the part of $\Delta\vec{D}$ resulting from the change in the rocket's aerodynamics depending on engine operation, while the term $\vec{D}_N^{off}$ stems from the fact that $\vec{D}_R^{on}$ and $\vec{D}_R^{off}$ are not the same force, since they are not acting on the same surfaces (the difference being the nozzle exit area $\partial\tau$).

2.5. National Aeronautics and Space Administration's Chemical Equilibrium with Applications (NASA CEA) programme

The National Aeronautics and Space Administration's (NASA) computer programme Chemical Equilibrium with Applications (CEA) was designed to calculate the chemical equilibrium compositions and properties of complex mixtures [8]. For this study, the theoretical rocket performance mode was utilised, knowing the product concentrations from the set of reactants that made up the propellant in the form of fuel and oxidiser. The thermodynamic and transport properties can be obtained for the product mixture at the exhaust of the motor. The motor uses a typical AP+HTPB+AL composition, with the exact composition being confidential.

3. CFD NUMERICAL SIMULATIONS

Since the rocket and its propulsion systems are essentially axisymmetric in nature, it was sufficient to perform 2D axisymmetric CFD simulations for the sake of this study (the only elements of the rocket that are not axisymmetric are the stabilising fins, which do not affect base drag in a meaningful way). To simplify the problem, it was assumed that the exhaust gases at the nozzle inlet are in a chemical equilibrium state (i.e. they are fully combusted). Moreover, Ansys® DesignModeler was used for preparing the geometry, Ansys® Mesher for meshing and defining the boundary conditions and Ansys® Fluent 20.2 for the numerical solution and post-processing.

3.1. Geometry

The considered geometry was prepared on the basis of the computer-aided design (CAD) model of the Grot sounding rocket and technical drawings of the nozzle (Fig. 5). Given that this case study involved an axisymmetric model, only half of the geometry was modelled in Ansys® DesignModeler. The outline of the Grot sounding rocket without fins in the axisymmetric view can be seen in Fig. 6.

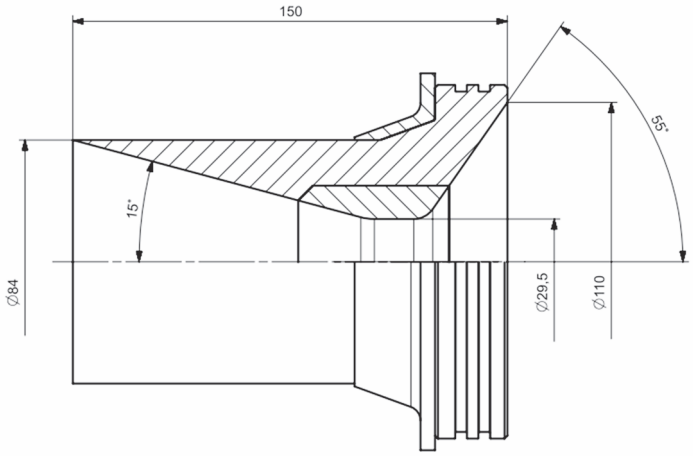


Figure 5. Technical drawing of Grot's nozzle.



Figure 6. Grot's shape outlines and domain regions in Ansys® DesignModeler.

In addition, a domain study was conducted in order to minimise and preferably eliminate the influence of domain size on the results; the selected domain size can be seen in Fig. 7.

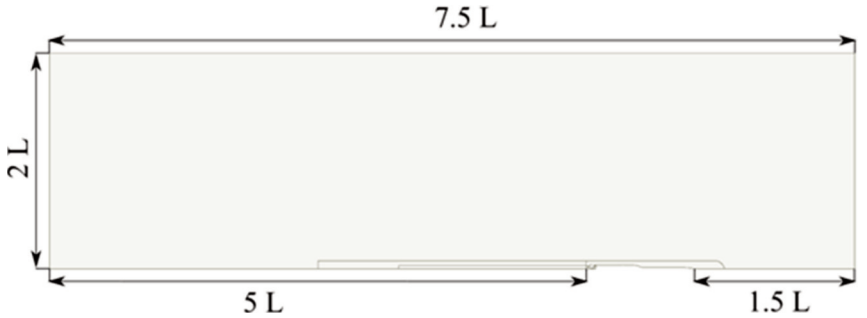


Figure 7. Fluid domain dimensions. *L* denotes the total length of the Grot sounding rocket.

3.2. Mesh

The overall quality of the mesh and the solver settings determine the accuracy of the results. However, the mesh used in a study may not require a large number of elements in order to obtain a fairly accurate solution. For this reason, a mesh independency study was conducted in order to determine the appropriate mesh settings so as to have minimal effect on the accuracy of results; as a result, the final mesh contained 626,458 elements. In addition, a structured mesh is favourable for increasing the efficiency of the calculations as it requires less memory. The nozzle and the plume region experience high gradients of pressure, temperature and Mach number; therefore, it was advantageous to utilise a dense-structured mesh in these areas; for this purpose, it was necessary for the fluid domain to be split into regions (Fig. 8).

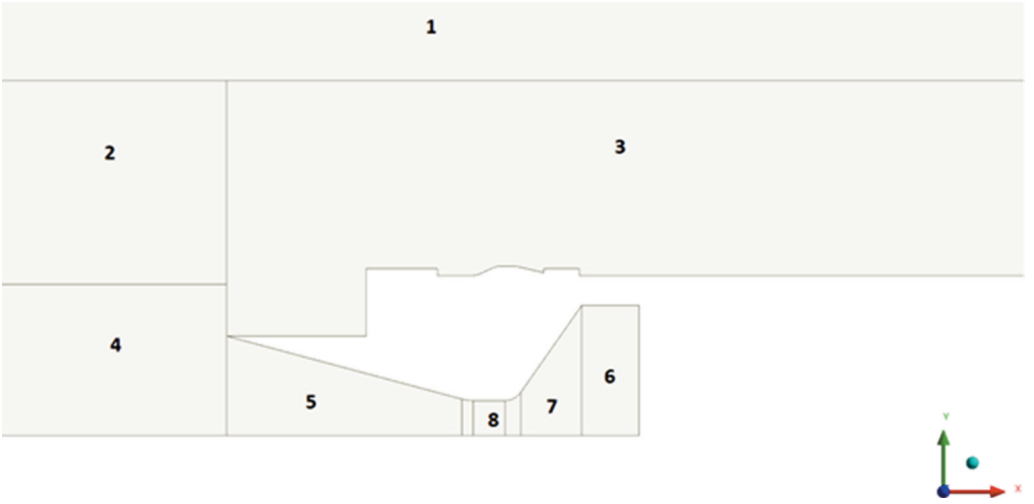


Figure 8. Fluid domain regions.

Secondly, performing external aerodynamic CFD simulations requires the modelling of the boundary layer during meshing; this is done in the form of inflation layers. For this to be done correctly, one must estimate the boundary layer thickness formed in the range of the Reynold numbers experienced during the flight of the vehicle [9] and model the inflation layers to contain the approximated boundary layer thickness. It was decided to keep the $30 \leq y^{+} \leq 300$ to implement the wall function approach for the shear stress transport (SST) k-ω turbulent model within Ansys® Fluent, as this provides a shorter calculation

time and lower number of mesh elements compared to $y^+ \leq 1$, while keeping the results relatively accurate. A similar choice of y+ has been observed in a previous paper [10]. For the nozzle, a bias factor was applied for capturing the boundary layer, followed with a dense mesh in the plume region. The mesh for the aforementioned domain regions was divided in the same manner (Figs 9 and 10).

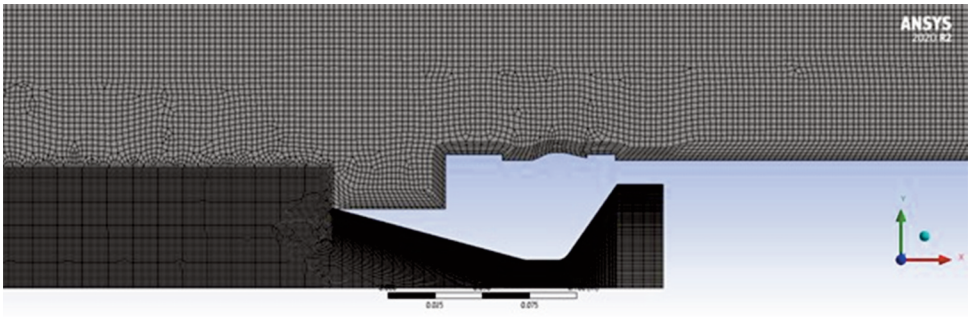


Figure 9. Near-nozzle mesh.

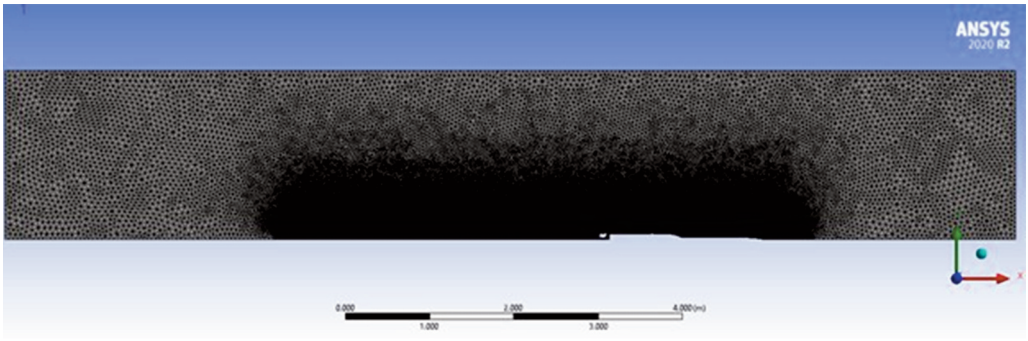


Figure 10. Global view of the mesh.

3.3. Solver setup

By using the NASA CEA software, the physical properties of the exhaust gases were obtained as a function of motor operation duration. For this case study, the input chamber pressure was known beforehand. This case study made use of the species transport model, since it models the interaction between the exhaust gases and the free-stream air. The motor operating point chosen for the aerodynamic analysis is the one providing the highest value of the thrust force.

Compressibility effects are prevalent when the fluid accelerates beyond Mach 0.3; thus, it was necessary to use the density-based solver in this study. As mentioned in Subsection 3.2, the SST k-ω turbulent model was utilised, which was found to be more favourable in previous works [10,11]; alongside the use of the energy equation, the ideal gas model was used, supplemented with the Sutherland model for viscosity. In addition, the second-order upwind scheme was chosen for all convective term flow variables as this provides higher accuracy. The study focuses on atmospheric conditions at sea level with a far-field pressure boundary condition at the domain inlet (p_a = 101,325 Pa and T_a = 288.15 K [15°C]). In addition, turbulent intensity was 2.16% and turbulent length scale was 0.012 m. Finally, solution steering and full multi-grid (FMG) initialisation [12] were both activated.

4. Results

4.1. CFD flow field results

For qualitative analysis of the obtained flow fields, the Mach number and static pressure, the contour plots for the operational and non-operational propulsion systems were analysed for the Mach number 1.2. The shock waves developed on the rocket appeared dimmer in the Mach number contour plot for the active motor than for the inactive motor (see Figs 11 and 12). This was due to the exhaust plume travelling at a Mach number three times greater than the free-stream air. Figures 13 and 14 present the static pressure for the same Mach number. Figures 15 and 16 show the closed-up static pressure contour plots for the aforementioned contour plots. It is important to note that the static pressure near the aft end (as defined by the red lines in Fig. 17) is lower in the engine-off case.

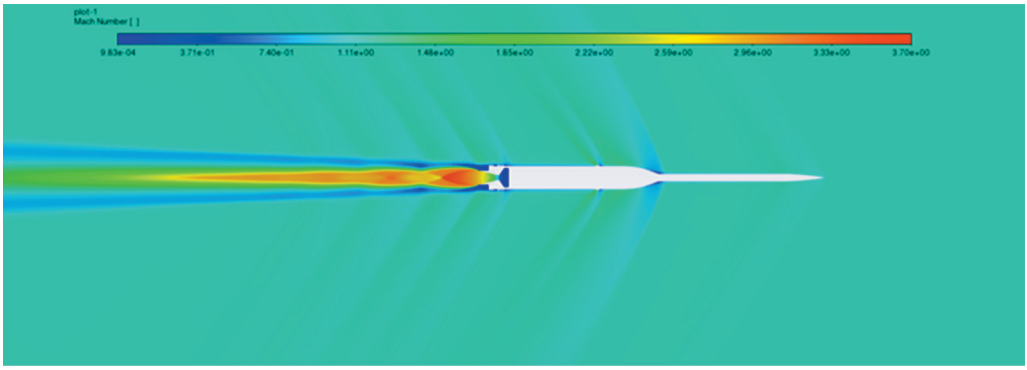


Figure 11. Contour plot of the local Mach number—active propulsion system, Mach 1.2.

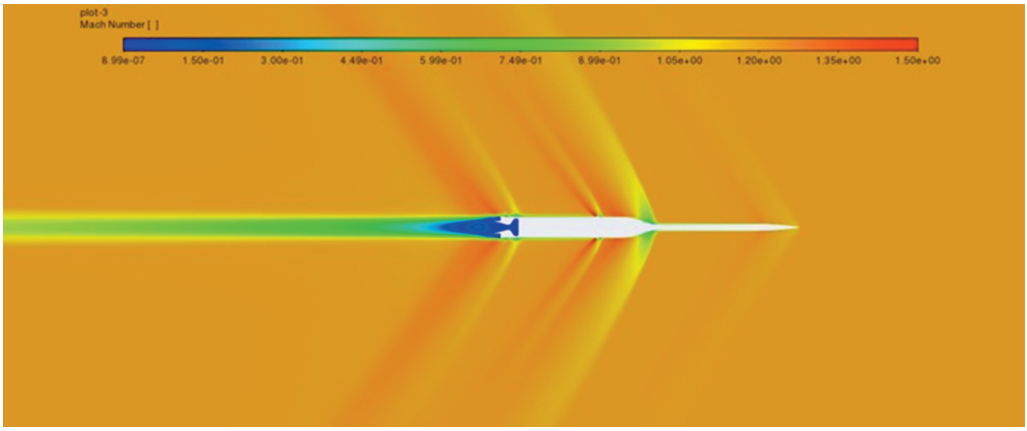


Figure 12. Contour plot of the local Mach number— inactive propulsion system, Mach 1.2.

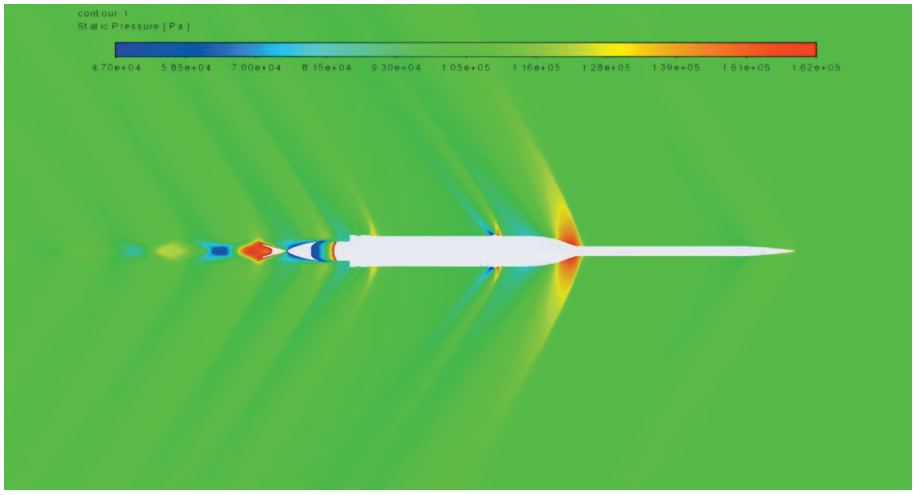


Figure 13. Contour plot of the local static pressure—active propulsion system, Mach 1.2.

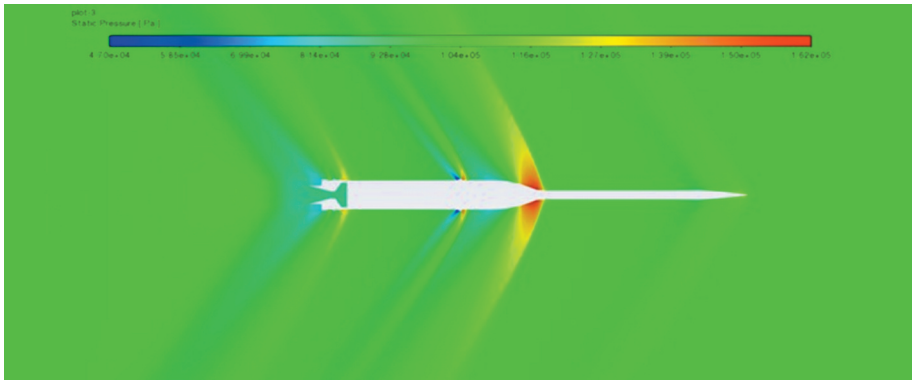


Figure 14. Contour plot of the local static pressure—inactive propulsion system, Mach 1.2.

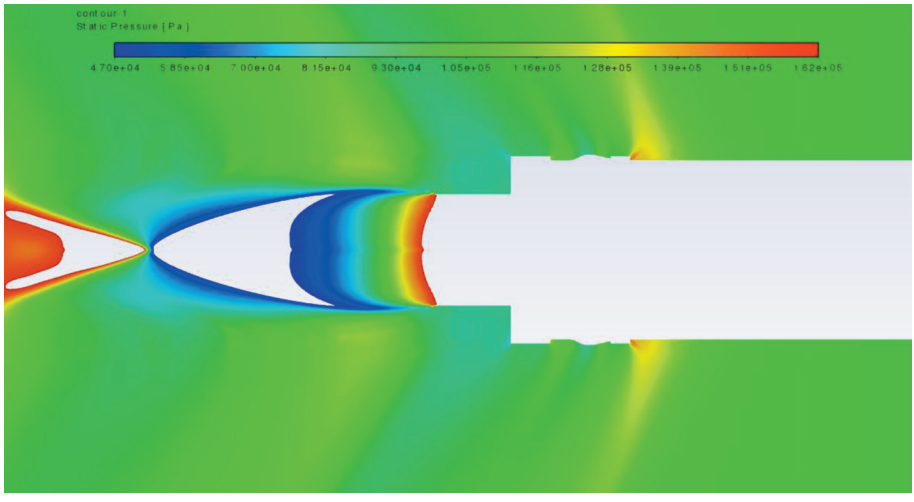


Figure 15. Contour plot of the local static pressure in the nozzle area—active propulsion system, Mach 1.2.

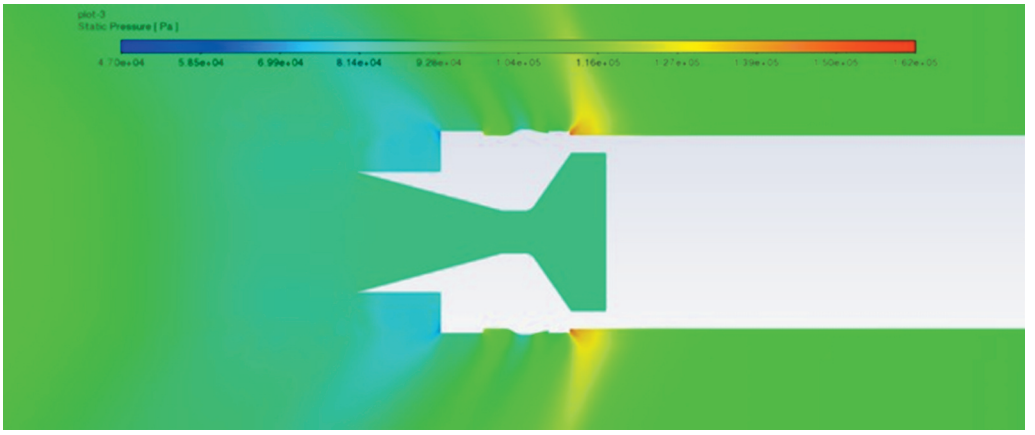


Figure 16. Contour plot of the local static pressure in the nozzle area—inactive propulsion system, Mach 1.2.

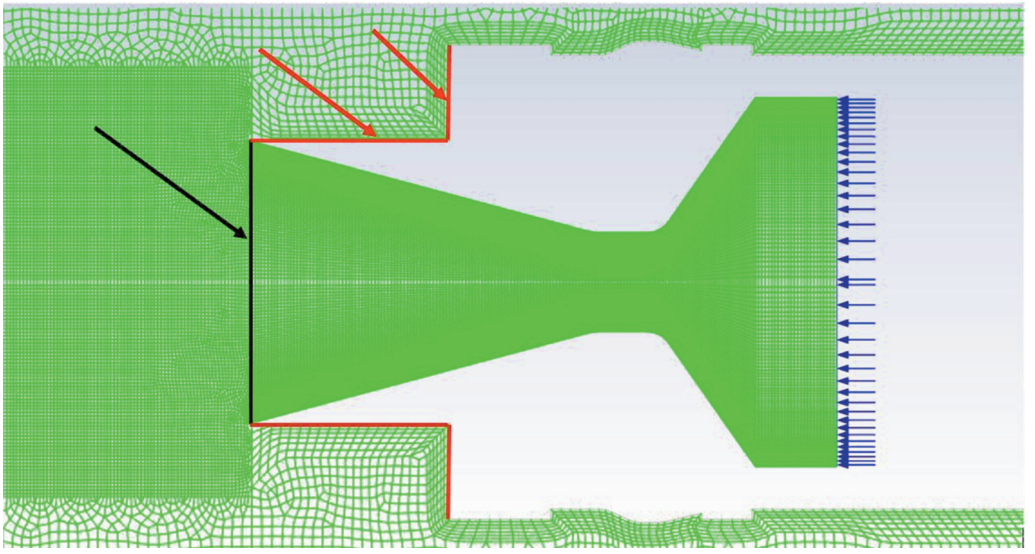


Figure 17. Areas of interest in the rear of the rocket. Black denotes the nozzle exit area, while red denotes the aft end.

4.2. Thrust values post-processing approach

To evaluate the thrust force, it was necessary to define the nozzle exit surface, as the calculations were made for an axisymmetric model. The exit surface of the nozzle is represented by a black line in Fig. 17.

The approach utilises the Ansys® Fluent post-processing surface integral reports and Eq. (3) presented in Subsection 2.3. However, to be able to use such an approach, one needs to define the inertial term from Eq. (3). For this purpose, a variable, $\rho \cdot \vec{v}_e \cdot |\vec{v}_e|$, representing the custom field variable is adopted. Afterwards, surface integrals of the custom field variable and the static pressure, which is the second term in Eq. (3), were calculated for the nozzle exit area. By summing up these two results, the thrust was obtained for each engine operating time step. As stated in Subsection 3.3, the maximum thrust operation point was utilised as the reference for the drag calculations, and this point gives a total effective thrust force of 7,750 N. As expected, the thrust value does not vary significantly with the Mach number.

4.3. Coefficients of axial forces of operational and non-operational propulsion systems

The raw data for the total drag coefficients for active and inactive propulsion systems, along with the difference between them, are presented in Table 2 and Figs 18 and 20.

Table 2. Computed drag coefficients.

M [–]	C_D^{on} [–]	C_D^{off} [–]	ΔC_D [–]
0.3	0.460	0.453	–0.007
0.6	0.378	0.457	0.079
0.8	0.359	0.462	0.100
1.0	0.494	0.668	0.170
1.2	0.628	0.744	0.120
1.6	0.577	0.659	0.080
2.0	0.506	0.576	0.070
2.5	0.435	0.495	0.060
3.0	0.383	0.429	0.046

M, free-stream Mach number; C_D^{on}, drag coefficient computed for the operating propulsion system; C_D^{off}, drag coefficient computed for the non-operating propulsion system; ΔC_D, difference between drag coefficients of operational and non-operational propulsion systems.

4.4. Base drag modelling

The total drag coefficients for both computational cases (active and inactive propulsion systems) are shown in Fig. 18. As expected, they are not equal; the difference is presented in Fig. 20. Further discussion of the results necessitates the introduction of some additional coefficients. The coefficient of drag acting on the nozzle exit (already defined in Eq. (6)) shall be denoted as $C_{D,N}^{off}$. In the case of the aft end, the drag coefficients for the engine-on and engine-off cases will be denoted as $C_{D,A}^{on}$ and $C_{D,A}^{off}$, respectively. In literature, both components (the drag acting on the nozzle exit and the aft end of the rocket) are being considered together and referred to as base drag. For the sake of comparison, the base drag coefficient of the Grot rocket can be defined as follows:

$$C_{D,B}^{on} = C_{D,A}^{on} \tag{11}$$

$$C_{D,B}^{off} = C_{D,A}^{off} + C_{D,N}^{off} \tag{12}$$

In Eq. (11), the pressure acting on the nozzle exit is not taken into account, since it is already a component of thrust, as defined by Eq. (4). The $C_{D,B}$ base drag coefficients computed during post-processing of the CFD study are directly compared with the analytical results obtained previously [4]

(Fig. 19). It can be noted that the curves are in relatively good agreement in the supersonic region, especially given that they are not describing exactly the same rocket. In the transonic region, the curves diverge, although this is mainly due to the analytical model being based on second-order supersonic flow solutions and thus being valid only in the supersonic domain.

The established $\Delta C_D(M)$ dependency does not seem to be easily modelled by simple physical models. However, it can be demonstrated that it can be fully described by two factors: the difference in taking into account the nozzle exit area (as explained in Subsubsection 2.4.2) and the change of pressure in the aft region. This hypothesis can be represented as follows:

$$\Delta C_D \approx C_{D,N}^{off} + C_{D,A}^{off} + C_{D,A}^{on}. \tag{13}$$

Indeed, the plot of both sides of the approximate equality in Fig. 21 proves that they are indeed almost identical. Consequently, it is confirmed that the influence of propulsion system operation on drag can be fully explained by the pressure acting on the aft end of the rocket.

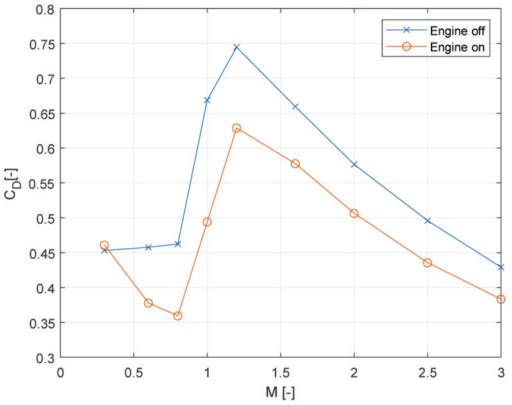


Figure 18. Total drag coefficient as a function of Mach number.

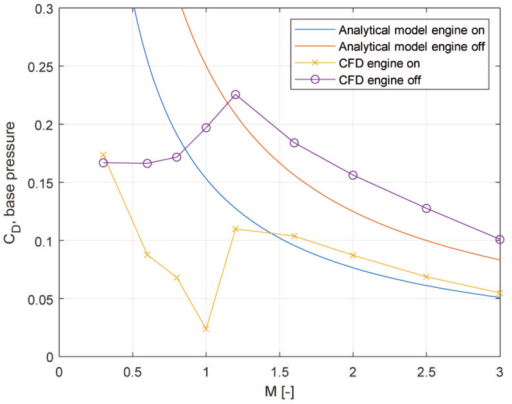


Figure 19. Comparison of base drag coefficients obtained by CFD and the analytical model found in [4].

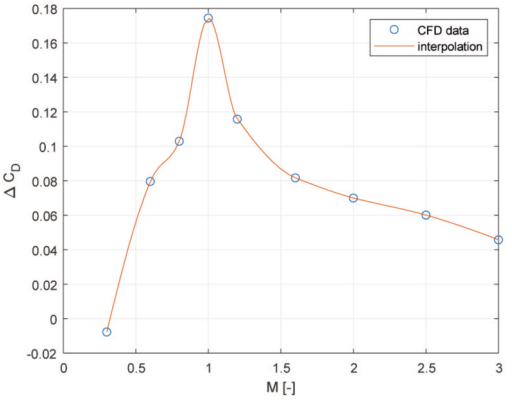


Figure 20. Difference in the total drag coefficient between active and inactive propulsion systems. Interpolation performed by the modified Akima method.

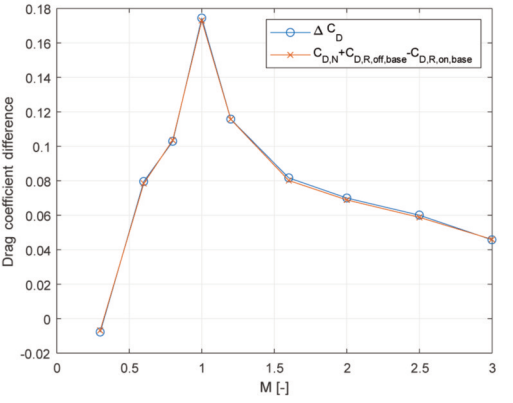


Figure 21. ΔC_D compared to the sum of engine-off nozzle exit pressure drag C^{off} and pressure change in the aft end due to engine operation.

4.5. Influence of altitude variation

Since the atmospheric parameters change with flight altitude, it is worth considering whether they affect the previously shown results. Additional numerical simulation for the flight altitude of 5 km was performed. For this altitude, the static pressure of 54,050 Pa and static temperature of 255.7 K (–17.45°C) were assumed. Figure 22 presents the comparison of ΔC_D between the results for this altitude and sea level. ΔC_D decreases with altitude in a proportional manner. The main reason for this difference is that the change in pressure and density influences the compressible behaviour of the flow. In addition, viscous effects are more pronounced due to the decrease of Reynolds number at a given Mach number for the 5 km case. However, upon analysing the CFD results, it became clear that the difference in viscous drag is negligible in comparison to the effects of pressure. Further analysis is required in order to model the dependence of ΔC_D on flight altitude.

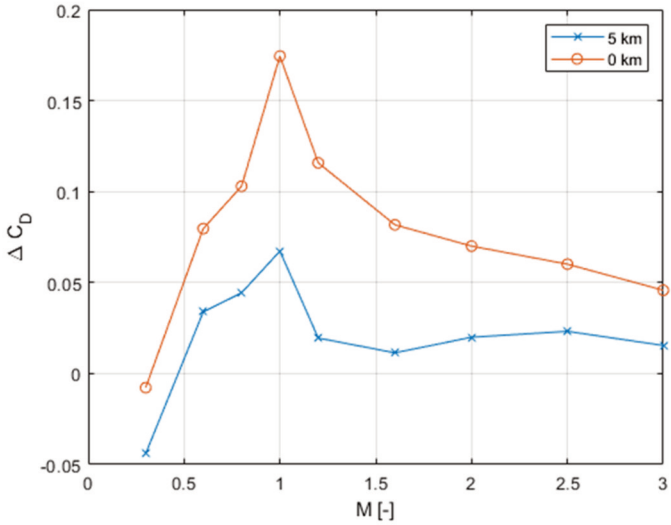


Figure 22. ΔC_D for altitudes of 0 km and 5 km.

5. CONCLUSIONS

Two series of axisymmetrical flow simulations of the Grot rocket were performed: one, with the propulsion system being inactive; and in the other, with the propulsion system operating with full thrust. The goal was to study and quantify the effect of motor operation on the rocket's drag coefficient. It has been demonstrated that drag is decreased during the thrusting phase. The dependence of the observed difference in drag coefficient on the Mach number has been found to be very non-linear and rather hard to approximate by a simple regressive model. For the sake of accurate flight simulation, it seems necessary to simply use interpolated CFD data. It has been shown that the analytical models of base drag found in a previous work [4] are in good agreement with the CFD results obtained in the supersonic domain. An important result is the proof that for all considered Mach numbers, the change in Grot's drag coefficient due to motor operation is fully described by the change of pressure forces acting on the nozzle exit and aft end regions. This conclusion holds despite Grot's non-standard geometry, with the nozzle extending noticeably from the aft end of the rocket. Therefore, it seems advisable to continue research on a general physical model for base drag prediction by attempting to link the base pressure with the rocket's velocity and basic propulsive parameters.

Acknowledgements: The authors would like to thank MESco Sp. z.o.o. and ANSYS Inc. for providing Ansys® Academic Mechanical and CFD licence. In addition, we would like to thank Mateusz Sochacki, M.Sc.Eng., from the Division of Automation and Aerospace Systems, Faculty of Power and Aeronautical Engineering, Warsaw University of Technology, for valuable remarks, which helped to improve this paper. This research was supported by a French Government Scholarship.

REFERENCES

[1] Gregorek, G.M. "Aerodynamic Drag of Model Rockets (TR-11)." Estes Industries, R&D 359-71. Penrose, Colorado, USA, 1970.

[2] Moore, F.G., Hymer, T.C. and Wilcox, J.W. "Improved Empirical Model for Base Drag Prediction on Missile Configurations Based on New Wind Tunnel Data." Naval Surface Warfare Center Dahlgren Division, AD-A258 753. Hampton, Virginia, USA, 1992.

[3] Brazzel, C.E. and Henerson, J.H. "A Correlation of the Base Drag of Bodies-of-Revolution with a Jet Exhausting through the Base." Army Missile Command, Redstone Arsenal, AD0634662. 1966.

[4] Huffman, M. "Sounding Rocket Redesign and Optimization for Payload Expansion and in Flight Telemetry Transmittal.", MSc thesis, University of Central Florida. Orlando, Florida, USA, 2005.

[5] Al-Obaidi, A.S.M. "Implementation of Semi-Empirical Models to Enhance the Accuracy of Panel Methods for Drag Prediction at Supersonic Speeds." *IIUM Engineering Journal* Vol. 12 No. 1 (2011): pp. 45–58.

[6] Kumar, V.S. "Estimation of Base Drag on Supersonic Cruise Missile." *International Research Journal of Engineering and Technology* Vol. 3 No. 1 (2016): pp. 662–665.

[7] Sutton, G.P. and Biblarz, Oscar. *Rocket Propulsion Elements*. 9th edn. John Wiley & Sons, Inc Hoboken, New Jersey, USA, 2016.

[8] Gordon, S. and McBride, B.J. Computer Program for Calculation of Complex Chemical Equilibrium Compo-Sitions and Applications. 1st edn. National Aeronautics and Space Administration, Office of Management, Scientific and Technical Information Program, Springfield, Virginia, USA, 1994.

[9] Çengel, Y.A. and Cimbala, J.M. Fluid Mechanics: Fundamentals and Applications. 3rd edn. McGraw Hill, New York, New York, USA, 2014.

[10] López, D., Domínguez, D. and Gonzalo, J. "Impact of Turbulence Modelling on External Supersonic Flow Field Simulations in Rocket Aerodynamics." *International Journal of Computational Fluid Dynamics* Vol. 27 No. 8–10 (2013): pp. 332–341.

[11] Aytaç, Z. and Aktas, F. "Utilization of CFD for the Aerodynamic Analysis of a Subsonic Rocket." *Politeknik Dergisi* Vol. 23 No. 3 (2020): pp. 879–887.

[12] Ansys, Inc. ANSYS Fluent User's Guide, Release 17. 2. 2016.